Check for updates

Controlled molecular assemblies of chiral boron dipyrromethene derivatives for circularly polarized luminescence in the red and near-infrared regions†

Hayato Sakai, [ID] *[a] Yudai Suzuki,[a] Makoto Tsurui,[b] Yuichi Kitagawa, [ID] [b] Takuya Nakashima, [ID] [cd] Tsuyoshi Kawai, [ID] [d] Yuta Kondo,[e] Go Matsuba, [ID] [e] Yasuchika Hasegawa [ID] *[b] and Taku Hasobe [ID] *[a]

Chiral 1,1′-bi-2-naphthol (BINOL)-substituted boron dipyrromethene (BODIPY) derivatives with different numbers of phenyl groups at the 2 and 6 positions (denoted as nPh-B-BODIPY; n = 0, 1, 2) were newly synthesized to examine the aggregation-enhanced emission and circularly polarized luminescence (CPL) in the red and near-infrared (NIR) regions. Upon injection of THF solution of nPh-B-BODIPY into H_2O, 0Ph-B-BODIPY underwent controlled self-assembly to produce fibrous nanoarchitectures, whereas spherical nanoparticles were formed in 1Ph-B-BODIPY and 2Ph-B-BODIPY. Absorption and CD spectra of 0Ph-B-BODIPY nanofibers demonstrated a red-shifted and split spectrum corresponding to the 0-0 band, suggesting strong interaction between neighbouring 0Ph-B-BODIPY units. Such fibrous assemblies exhibited a broad emission spectrum with multiple bands ranging from the visible to the near-infrared (NIR) region due to the multiple aggregate states. Consequently, 0Ph-B-BODIPY nanofibers demonstrated a broad circularly polarized luminescence (CPL) spectrum in the red to NIR regions together with the enhanced dissymmetry factors (g_{lum}) relative to 0Ph-B-BODIPY (monomer) and 1Ph-B-BODIPY nanoparticles.

Introduction

Circularly polarized light is widely utilized in various fields such as three-dimensional (3D) displays, biological probes and tags and spintronic devices.[1–5] In particular, many research examples of circular dichroism (CD) and circularly polarized luminescence (CPL) using small organic molecules and metal–organic materials

[a] *Department of Chemistry, Faculty of Science and Technology, Keio University, 3-14-1 Hiyoshi, Yokohama, Kanagawa 223-8522, Japan.*
E-mail: hasobe@chem.keio.ac.jp, sakai@chem.keio.ac.jp

[b] *Faculty of Engineering and Institute for Chemical Reaction Design and Discovery (WPI-ICReDD), Hokkaido University, Sapporo, Hokkaido 060-8628, Japan.*
E-mail: hasegaway@eng.hokudai.ac.jp

[c] *Department of Chemistry, Graduate School of Science, Osaka Metropolitan University, Sumiyoshi, Osaka 558-8585, Japan*

[d] *Division of Materials Science, Nara Institute of Science and Technology, Ikoma, Nara 630-0192, Japan*

[e] *Graduate School of Organic Materials Science, Yamagata University, Yonezawa, Yamagata 992-8510, Japan*

† Electronic supplementary information (ESI) available: Synthetic details, ^{1}H NMR and ^{13}C NMR spectra, MALDI-TOF mass spectra, steady-state absorption and fluorescence spectra, dynamic light scattering measurements, XRD patterns, SAXS profiles, crystallographic details, and CD spectra. CCDC 1993841, 1993847 and 1993848. For ESI and crystallographic data in CIF or other electronic format see DOI: https://doi.org/10.1039/d2tc05006d

have been reported so far.[6–15] In this regard, we have reported the syntheses and chiroptical properties of donor–acceptor-type helicene derivatives to improve the absorption properties in the visible region and corresponding fluorescence quantum yields.[16–21] Among the reported small organic molecular systems for CPL, the number of CPL systems in the near-infrared (NIR) region is limited as compared to those in the visible region.[21–26] The main reasons include the synthetic difficulties of chiral molecules with large π-extended and small HOMO–LUMO gaps. The extended π-conjugation is a direct way for improving absorption and fluorescence properties in the NIR region. However, the degree of red-shift trend by this strategy is quite small in the case of chiral carbohelicene, a typical chiral molecule.[27–29] For example, [16]carbohelicene demonstrated an absorption maximum at *ca.* 430 nm corresponding to a 0-0 transition.[30]

Boron-dipyrromethene (BODIPY) dyes are one of the representative small organic luminophores with high fluorescence quantum yields (Φ_{FL}) because these derivatives are typically utilized in various research fields such as biological, medical, and electronic applications.[31–37] Formation of molecular aggregation in a mixed solvent is a plausible way of observing red and NIR luminescence together with aggregation-induced emission (AIE).[38,39] Furthermore, the aggregate formation of BODIPYs substituted by aryl units at 2 and/or 6 positions in a mixed

This journal is © The Royal Society of Chemistry 2023

J. Mater. Chem. C, 2023, 11, 2889–2896 | **2889**

Fig. 1 Chemical structures of *n*Ph-B-BODIPY derivatives and a reference compound in this study.

solution exhibited the broad fluorescence spectra across red and NIR regions because of domino-like multi-emission processes.[40] However, no attention has been drawn toward the aggregation-enhanced CPL properties in the NIR region, whereas the chiroptical properties of these BODIPY derivatives were reported.[7,21,41–44] Additionally, the formation of nanobubbles in aqueous THF solution has attracted much interest in recent years[45–48] and the relevance between nanobubbles and molecular aggregate structures is interesting considering the many examples of molecular aggregates in H_2O/THF mixtures.[49]

Based on the above contents, in this study, we newly designed and synthesized a series of 1,1′-bi-2-naphthol (BINOL)-substituted BODIPY derivatives (*n*Ph-B-BODIPY) with different numbers of phenyl groups (n = 0, 1, 2) at the 2 and 6 positions to investigate the aggregation-enhanced spectroscopic and chiroptical properties of chiral BODIPY derivatives in the red and NIR regions (Fig. 1). An appropriate steric hindrance at the 2 and 6 positions of a BODIPY unit largely has an effect on the aggregate structures in the H_2O/THF mixture, which results in the enhanced spectroscopic and chiroptical properties. In addition to the absorption and CD properties in the visible region, the aggregate trends of fibrous BODIPY assemblies enhanced the broad fluorescence spectra and corresponding CPL properties in the red and NIR regions. Finally, these emission processes were kinetically discussed by time-resolved fluorescence spectra.

Experimental section

General methods

All solvents and reagents of the best grade available were purchased from commercial suppliers such as the Tokyo Chemical Industry, Nacalai Tesque, Wako Pure Chemical Industries and Sigma-Aldrich. All commercial reagents were used without further purification. Column flash chromatography was performed on silica gel (Fuji Silysia Chemical LTD, 40–50 μm or 100–210 μm). ^{1}H NMR and ^{13}C NMR spectra were recorded on an AL-400, or an ALPHA-400 spectrometer using the solvent peak as the reference standard, with chemical shifts given in parts per million. CDCl$_3$ was used as the NMR solvent. MALDI-TOF mass spectra were recorded on a JEOL JMS-S3000 spectrometer.

Spectroscopic measurements

UV-vis absorption spectra were recorded on a PerkinElmer (Lamda 750) UV-VIS-NIR spectrophotometer. Fluorescence spectra and absolute fluorescence quantum yields are measured on a JASCO FP-8500 spectrophotometer. Fluorescence lifetimes were also measured on a HORIBA Scientific time-correlated single-photon counting system (FluoroCube) with a laser light (Delta-Diode, laser diode head) as an excitation source. The laser operation wavelength, pulse width, and frequency were 404 nm, 50 ps and 1 MHz, respectively. The practical time resolution is 15 ps by deconvolution of an observed trace with the analytical software (DAS6). CD spectra were recorded on a JASCO J-725 spectropolarimeter. CPL spectra were recorded on a JASCO CPL-300 spectro-fluoropolarimeter.

Dynamic light scattering (DLS) measurements

The particle size and distribution were measured in H_2O/THF = 99/1 (v/v), using light-scattering equipment (Zetasizer nano ZS).

TEM measurements

Transmission electron micrograph (TEM) measurements were recorded on a Tecnai TEM-120 (FEI company) by applying a drop of the sample to a copper grid. TEM images were recorded on a transmission electron microscope at an accelerating voltage of 120 kV for imaging.

Preparation and analysis of single crystal structures

Single crystals for packing formation analysis were obtained from toluene and methanol solution for *R*-0Ph-B-BODIPY, THF and hexane solution for *R*-1Ph-B-BODIPY, and toluene and methanol solution for *R*-2Ph-B-BODIPY using a conventional vapor-diffusion method. Crystal data were collected on a Rigaku R-AXIS RAPID diffractometer with graphite-mono-chromated MoKa radiation. The structures were solved by direct methods (SHELXS-97). Molecular graphics were generated with ORTEP-3 for Windows. Additional crystallographic information is available in the ESI.† CCDC 1993841 (*R*-0Ph-B-BODIPY), CCDC 1993847 (*R*-1Ph-B-BODIPY) and CCDC 1993848 (*R*-2Ph-B-BODIPY) contains the supplementary crystallographic data for this paper.†

2890 | *J. Mater. Chem. C*, 2023, **11**, 2889–2896

This journal is © The Royal Society of Chemistry 2023

Results and discussion

Synthesis

Parent BODIPY dyes without BINOL such as BODIPY-ref were synthesized following the reported method[50] (Fig. 1). A series of BINOL-substituted BODIPY derivatives such as nPh-B-BODIPY (n = 0, 1, 2) (Fig. 1) was synthesized by exchanging fluorine in the parent BODIPY with chiral BINOL as shown in Schemes S1–S3 in the (ESI†). Note that the bromine units were substituted at the 6,6′-positions of BINOL as an electron with-drawing group to improve the fluorescence properties. These derivatives were well-characterized via ^{1}H NMR spectroscopy, ^{13}C NMR spectroscopy and high-resolution MALDI-TOF mass spectrometry (see the Fig. S1–S9 in the ESI†). The absolute configuration of nPh-B-BODIPY (n = 0, 1, 2) with the chiral BINOL unit was determined by single crystal X-ray analyses and CD measurements.[7,51] The configuration of BINOL remained unchanged in nPh-B-BODIPY (n = 0, 1, 2).

Preparation and structural analysis of molecular assemblies of B-BODIPY derivatives

The preparation of molecular assemblies of chiral B-BODIPY derivatives was as follows. These B-BODIPY derivatives are highly soluble in THF, but completely insoluble in H_2O. The proper choice of these solvents enables obtaining the con-trolled molecular aggregates. In particular, the mode of mixing is an important factor to achieve the desired sizes and shapes of B-BODIPY assemblies. To optimize the experimental condi-tions, we performed the concentration-dependent (Fig. S10 in the ESI†) and solvent volume ratio-dependent spectroscopic measurements using absorption and fluorescence spectra (Fig. S11–S14 in the ESI†). The optimized concentration of B-BODIPY is 30 μM in H_2O/THF = 99/1 (v/v). Trans-mission electron microscope (TEM) images of optimized 0Ph-B-BODIPY, 1Ph-B-BODIPY and 2Ph-B-BODIPY assemblies [denoted as (0Ph-B-BODIPY)$_m$, (1Ph-B-BODIPY)$_m$ and (2Ph-B-BODIPY)$_m$] are shown in Fig. 2. (0Ph-B-BODIPY)$_m$ demonstrated fibrous structures, which are in sharp contrast to the spherical nanoparticles of (1Ph-B-BODIPY)$_m$ and (2Ph-B-BODIPY)$_m$. The width of (0Ph-B-BODIPY)$_m$ is ca. 27.8 ± 6.4 nm, whereas the diameters of (1Ph-B-BODIPY)$_m$ and (2Ph-B-BODIPY)$_m$ are ca. 133 ± 49 nm and ca. 104 ± 22 nm, respectively (Fig. S15 in the ESI†). These diameters of (1Ph-B-BODIPY)$_m$ and (2Ph-B-BODIPY)$_m$ approximately agreed with the estimated sizes by dynamic light scattering (DLS) measurements such as 129 nm in (1Ph-B-BODIPY)$_m$ and 110 nm in (2Ph-B-BODIPY)$_m$ (Fig. S16 in the ESI†). These differences in aggregate structures are likely due to the steric hindrance of the phenyl groups modified on the BODIPY unit (vide infra).

To discuss the internal packing structures, first, single crystal structures of BODIPY derivatives were measured (Fig. 3 and Fig. S17 and S18 and Tables S1–S3 in the ESI†). We prepared single crystals of BODIPY derivatives for X-ray diffraction analysis by the vapor diffusion procedure at room temperature (see the ESI†), and the crystal data are summarized in Tables S1–S3 in the ESI.† 0Ph-B-BODIPY exhibits one-dimensional packing formation along
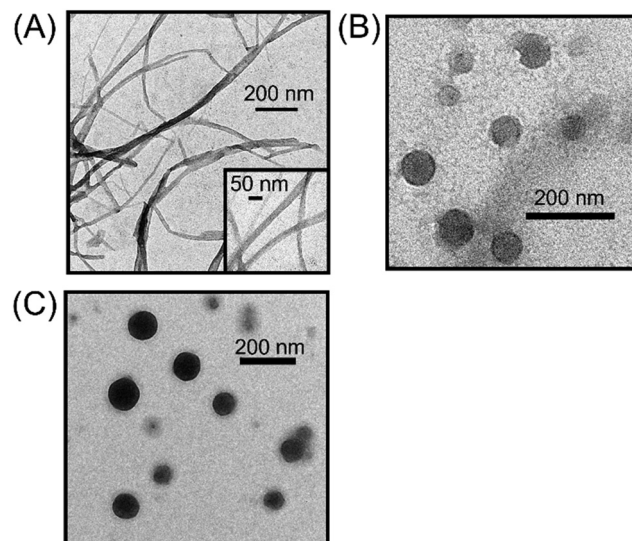

Fig. 2 TEM images of (A) (0Ph–B–BODIPY)$_m$, (B) (1Ph–B–BODIPY)$_m$, and (C) (2Ph–B–BODIPY)$_m$ prepared in H_2O/THF = 99/1 (v/v).
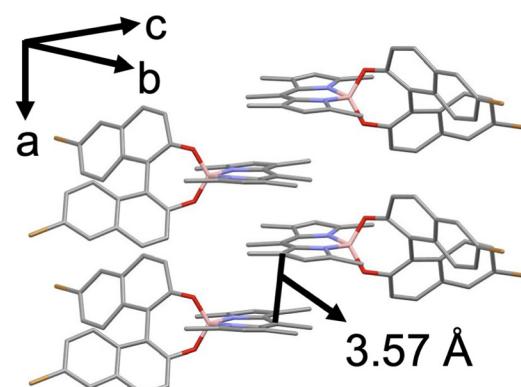
Fig. 3 Single-crystal structures of π-stacking between two neighbouring R-0Ph-B-BODIPY units. Black line: π-stacking distance: 3.57 Å.

the crystallographic a axis by virtue of intercolumnar interaction between two nearby BODIPY units (Fig. 3). The BINOL units were alternately arranged in the same column. Such an aligned π-stacking formation is responsible for the aggregation trend in spectroscopic measurements (vide infra). 1Ph-B-BODIPY and 2Ph-B-BODIPY also formed columnar structures with one-dimensional packing formation along the crystallographic a or b axis, with BINOL units alternating within the same column (Fig. S17 and S18 in the ESI†). The distance between adjacent BODIPY units in 1Ph-B-BODIPY and 2Ph-B-BODIPY are 3.60 Å and 3.68 Å, respectively, which are larger than that in 0Ph-B-BODIPY. This is probably attributed to the steric hindrance of the phenyl group in the BODIPY unit.

Then, to examine the internal structures of (nPh-B-BODIPY)$_m$, we also compared the X-ray diffraction (XRD) pat-terns of (nPh-B-BODIPY)$_m$. In Fig. S19 in the ESI,† patterns a and b are the XRD pattern obtained from (0Ph-B-BODIPY)$_m$ and the simulated one from the crystal structure of 0Ph-B-BODIPY,

This journal is © The Royal Society of Chemistry 2023

J. Mater. Chem. C, 2023, 11, 2889–2896 | 2891

respectively. Although relatively broad XRD peaks are observed due to the aggregates containing amorphous structures, they are roughly consistent with the simulated patterns from the single crystals. This suggests that the internal alignments of fibrous assemblies are similar to those of the crystal structures. In addition, we can see the strong diffraction peaks of b- and c-axes such as (012) and (023) as shown in the pattern a of Fig. S19 in the ESI.† In contrast, diffractions based on the a-axis were very weak in intensity. Considering the unit cell structure (orthorhombic crystal: dihedral angles of a–c and b–c axes: 90°), the growth direction of fibrous assemblies is in the direction of the a-axis. This means that the continuously stacked formation of BODIPY units in $(0Ph\text{-}B\text{-}BODIPY)_m$ forms macroscopic fibrous structures. This is in sharp contrast to the absence of XRD peaks in $(1Ph\text{-}B\text{-}BODIPY)_m$ and $(2Ph\text{-}B\text{-}BODIPY)_m$ (*i.e.*, amorphous structures). Additionally, the radius value of gyration in $(0Ph\text{-}B\text{-}BODIPY)_m$ estimated by small-angle X-ray scattering (SAXS) is comparable to the value estimated in the TEM image (Fig. 2A). The discussions are briefly stated in Fig. S20 in the ESI.†

Steady-state spectroscopic measurements

Steady-state spectroscopic measurements of optimized B-BODIPY assemblies such as $(0Ph\text{-}B\text{-}BODIPY)_m$, $(1Ph\text{-}B\text{-}BODIPY)_m$ and $(2Ph\text{-}B\text{-}BODIPY)_m$ were performed (Fig. 4 and Fig. S21 and S22 in the ESI†). The absorption and CD spectra of $(0Ph\text{-}B\text{-}BODIPY)_m$ and $0Ph\text{-}B\text{-}BODIPY$ (monomer) were measured as shown in Fig. 4A and 4B. The spectra of $(1Ph\text{-}B\text{-}BODIPY)_m$ and $1Ph\text{-}B\text{-}BODIPY$ are shown in Fig. S21 in the ESI,† together with those of $(2Ph\text{-}B\text{-}BODIPY)_m$ and $2Ph\text{-}B\text{-}BODIPY$ (Fig. S22 in the ESI†). The absorption spectrum of $(0Ph\text{-}B\text{-}BODIPY)_m$ prepared in $H_2O/THF = 99/1$ (v/v) (spectrum a in Fig. 4A) became much broadened and red-shifted as compared to the corresponding monomer ($0Ph\text{-}B\text{-}BODIPY$) in THF (spectrum b). The original absorption maximum of $0Ph\text{-}B\text{-}BODIPY$ at 499 nm was found as split peaks for $(0Ph\text{-}B\text{-}BODIPY)_m$ at 461 and 506 nm, due to the exciton coupling. In contrast, the reduced broadened and red-shifted trends without split peaks were seen in $(1Ph\text{-}B\text{-}BODIPY)_m$ (Fig. S21A in the ESI†) and $(2Ph\text{-}B\text{-}BODIPY)_m$ (Fig. S22A in the ESI†). These differences may be attributable to the smaller steric hindrance of $0Ph\text{-}B\text{-}BODIPY$ than those of $1Ph\text{-}B\text{-}BODIPY$ and $2Ph\text{-}B\text{-}BODIPY$ as discussed in single crystal structures (Fig. 3 and Fig. S17–S18 in the ESI†) (*vide supra*). Fig. 4B shows the CD spectra of $(0Ph\text{-}B\text{-}BODIPY)_m$ and a corresponding monomer: $0Ph\text{-}B\text{-}BODIPY$. The enantiomers such as $R\text{-}0Ph\text{-}B\text{-}BODIPY$ and $S\text{-}0Ph\text{-}B\text{-}BODIPY$ exhibit mirror-image Cotton effects in the UV and visible regions. The $\Delta\varepsilon$ of $0Ph\text{-}B\text{-}BODIPY$ in the UV region (162 M^{-1} cm^{-1} at 224 nm) was much larger than that in the visible region (59 M^{-1} cm^{-1} at 499 nm). In contrast, in the case of $(0Ph\text{-}B\text{-}BODIPY)_m$, we can observe a broadened CD spectrum together with the larger $\Delta\varepsilon$ in the visible region (*e.g.*, 122 M^{-1} cm^{-1} at 443 nm). Thus, the absorption dissymmetry factors (g_{abs}) of the S form in $(0Ph\text{-}B\text{-}BODIPY)_m$ were calculated to be $+2.52 \times 10^{-3}$ at 264 nm, $+5.30 \times 10^{-3}$ at 439 nm and $+1.44 \times 10^{-3}$ at 485 nm (Fig. 4C). These values are comparable in the monomeric form: $0Ph\text{-}B\text{-}BODIPY$ ($+5.66 \times 10^{-3}$ at 262 nm, $+8.93 \times 10^{-4}$ at 455 nm and
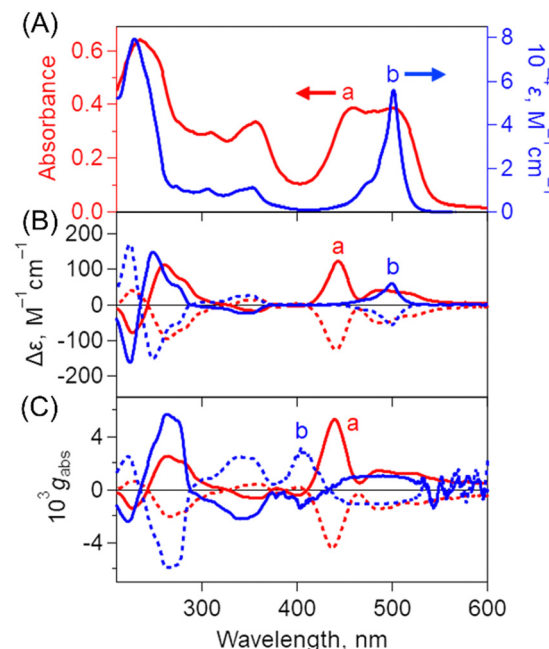
Fig. 4 (A) Absorption spectra of (a) $(0Ph\text{-}B\text{-}BODIPY)_m$ in $H_2O/THF = 99/1$ (v/v). $[0Ph\text{-}B\text{-}BODIPY] = 30$ μM and (b) $0Ph\text{-}B\text{-}BODIPY$ in THF. (B) CD spectra of (a) $(0Ph\text{-}B\text{-}BODIPY)_m$ in $H_2O/THF = 99/1$ (v/v). $[0Ph\text{-}B\text{-}BODIPY] = 30$ μM and (b) $0Ph\text{-}B\text{-}BODIPY$ in THF. Solid and dotted lines correspond to S and R forms, respectively. (C) Dissymmetry factor g_{abs} profiles of (a) $(0Ph\text{-}B\text{-}BODIPY)_m$ in $H_2O/THF = 99/1$ (v/v). $[0Ph\text{-}B\text{-}BODIPY] = 30$ μM in H_2O/THF and (b) $0Ph\text{-}B\text{-}BODIPY$ in THF. Solid and dotted lines correspond to S and R forms, respectively.

$+1.00 \times 10^{-3}$ at 501 nm). The emphasis is on the significant increase of the g_{abs} values in $(0Ph\text{-}B\text{-}BODIPY)_m$ in the visible region. Although similar enhanced trends of g_{abs} values in the visible region were observed in $(1Ph\text{-}B\text{-}BODIPY)_m$ (Fig. S21C in the ESI†) and $(2Ph\text{-}B\text{-}BODIPY)_m$ (Fig. S22C in the ESI†), the degree of the enhancement of $(0Ph\text{-}B\text{-}BODIPY)_m$ relative to the monomer is much larger than those of $(1Ph\text{-}B\text{-}BODIPY)_m$ and $(2Ph\text{-}B\text{-}BODIPY)_m$. Furthermore, in contrast with $(1Ph\text{-}B\text{-}BODIPY)_m$ and $(2Ph\text{-}B\text{-}BODIPY)_m$, $(0Ph\text{-}B\text{-}BODIPY)_m$ demonstrated two split CD Cotton effects at around 400–550 nm, suggesting stronger interaction between chromophore units.

Fig. 5A shows fluorescence spectra of $(0Ph\text{-}B\text{-}BODIPY)_m$ in $H_2O/THF = 99/1$ (v/v). In contrast to the sharp fluorescence spectrum of $0Ph\text{-}B\text{-}BODIPY$ (monomer) with a maximum at 531 nm, $(0Ph\text{-}B\text{-}BODIPY)_m$ exhibited a much broader spectrum with maxima at 503, 542, 610, 655 and 700 nm. $(0Ph\text{-}B\text{-}BODIPY)_m$ demonstrated a broad emission spectrum with multiple bands in the visible and NIR regions, which strongly suggested a possibility of multiple aggregate states (*vide infra*). The similar red-shifted trends relative to these corresponding monomers were observed for $(1Ph\text{-}B\text{-}BODIPY)_m$ and $(2Ph\text{-}B\text{-}BODIPY)_m$, although the degree was considerable smaller as compared to $(0Ph\text{-}B\text{-}BODIPY)_m$. This is probably because of the larger steric hindrance of the phenyl groups at the 2 and 6 positions of the BODIPY unit (Fig. 5B and Fig. S23 in the ESI†). The detailed absolute fluorescence quantum yields (Φ_{FL}) of $(0Ph\text{-}B\text{-}BODIPY)_m$, $(1Ph\text{-}B\text{-}BODIPY)_m$, and $(2Ph\text{-}B\text{-}BODIPY)_m$

2892 | *J. Mater. Chem. C*, 2023, **11**, 2889–2896

This journal is © The Royal Society of Chemistry 2023
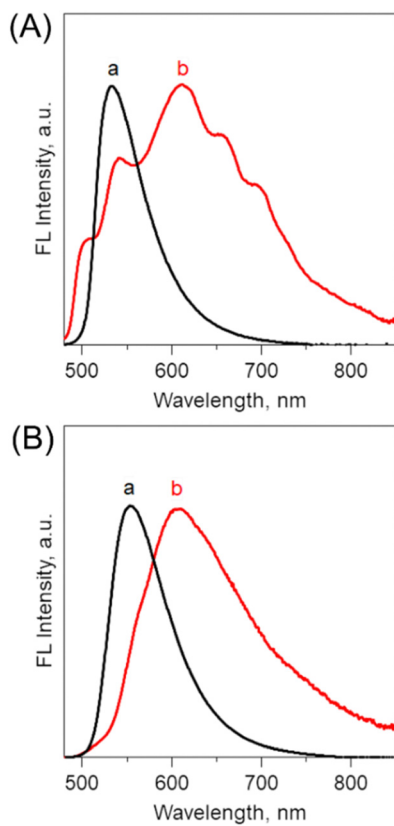
Fig. 5 Fluorescence spectra of (A) (a) 0Ph-B-BODIPY (monomer: black) in THF and (b) (0Ph-B-BODIPY)$_m$ in H$_2$O/THF = 99/1 (v/v) (red) and (B) (a) 1Ph-B-BODIPY (monomer: black) in THF and (b) (1Ph-B-BODIPY)$_m$ in H$_2$O/THF = 99/1 (v/v) (red), λ_{ex}: 470 nm.

and the corresponding monomers are shown in Table 1. In B-BODIPY monomers, the values of Φ_{FL} increased with increasing the number of phenyl groups substituted onto the BODIPY unit, which is attributed to the improvement of the intra-molecular charge transfer (ICT) properties of B-BODIPY with the introduction of phenyl groups.[52] In contrast, the Φ_{FL} values for these three assemblies are larger than those for the corresponding monomers. The plausible reason includes the aggregation-induced emission (AIE) of these B-BODIPY derivatives as stated above. The emphasis is on the significant enhancement of (0Ph-B-BODIPY)$_m$ (Φ_{FL} = 0.40) relative to 0Ph-B-BODIPY (Φ_{FL} = 0.025). This is in sharp contrast to (1Ph-B-BODIPY)$_m$ and (2Ph-B-BODIPY)$_m$ as shown in Table 1. Then, the CPL spectra and corresponding dissymmetry factors (g_{lum}) were investigated as shown in Fig. 6 and Fig. S24 in the ESI.†

Table 1 Summarized absolute fluorescence quantum yields of B-BODIPY derivatives (λ_{ex}: 470 nm)

	Φ_{FL} (assembly)[a]	Φ_{FL} (monomer)[b]
0Ph-B-BODIPY	0.40	0.025
1Ph-B-BODIPY	0.87	0.24
2Ph-B-BODIPY	0.95	0.89

[a] measured in H$_2$O/THF = 99/1 (v/v). [b] measured in THF.

Associated with the above-mentioned broadened fluorescence spectra, the CPL spectra of (0Ph-B-BODIPY)$_m$ largely extended up to the NIR region as compared to those of the monomeric forms (Fig. 6A). An approximately mirrored CPL signal was observed, but not perfectly symmetrical. Since the measurements were performed in aggregate states, inevitably there are small differences in the spectral shapes.[53,54] The g_{lum} value of S-(0Ph-B-BODIPY)$_m$ is estimated to be *ca.* -5.9×10^{-3} at 638 nm, which is about three times larger than its value for R-0Ph-B-BODIPY (monomer) (g_{lum} = *ca.* -2.1×10^{-3} at 545 nm) (Fig. S24A and S24B in the ESI†). It is also interesting to note that the positive and negative CPL spectra between (0Ph-B-BODIPY)$_m$ and 0Ph-B-BODIPY were shown in opposite directions. In contrast with the positive CPL signal of S-0Ph-B-BODIPY, we can see the negative direction in (S-0Ph-B-BODIPY)$_m$. According to recent reports,[55–57] this is probably due to the conformational changes caused by molecular aggregates and/or different torsion angles of binaphthyl units in the excited and ground states. In contrast, the signs of CPL in 0Ph-B-BODIPY agree with those of CD at the lowest-energy band, which agrees with the general trends for the CD and CPL spectra. Such a positive and negative inversion in the CD and CPL signals was observed only in (0Ph-B-BODIPY)$_m$ (Fig. 6B). The g_{lum} values slightly decreased with increasing the
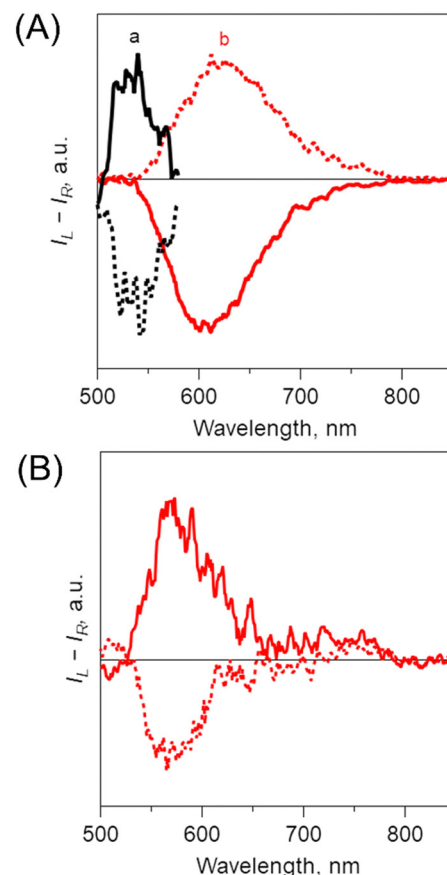
Fig. 6 (A) Circularly polarized luminescence (CPL) spectra of (a) 0Ph-B-BODIPY (monomer) in THF and (b) (0Ph-B-BODIPY)$_m$ in H$_2$O/THF = 99/1 (v/v), λ_{ex}: 350 nm. (B) R-(1Ph-B-BODIPY)$_m$ in H$_2$O/THF = 99/1 (v/v), λ_{ex}: 350 nm. Solid and dotted lines correspond to S and R forms, respectively.

This journal is © The Royal Society of Chemistry 2023

J. Mater. Chem. C, 2023, **11**, 2889–2896 | **2893**
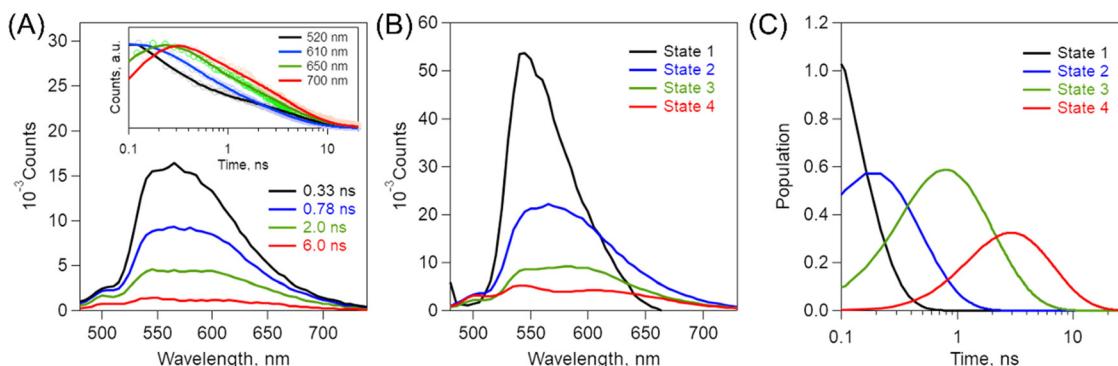
Fig. 7 (A) Time-resolved fluorescence spectra of (0Ph–B–BODIPY)$_m$ in H$_2$O/THF = 99/1 (v/v), λ_{ex}: 404 nm. Inset shows corresponding time profiles at 520 (black), 610 (blue), 650 (green), and 700 nm (red). (B) Species-associated spectra (SAS) of (0Ph–B–BODIPY)m in H$_2$O/THF = 99/1 (v/v) as obtained by target analysis of the time-resolved fluorescence spectra. (C) Corresponding population kinetics.
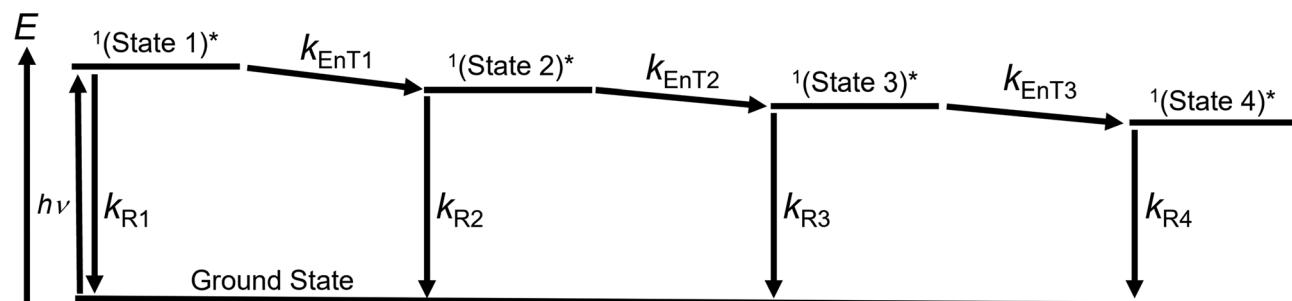
Scheme 1 Proposed kinetic models for emission processes from multiple aggregate states and related processes in (0Ph–B–BODIPY)$_m$.

volume ratios between H$_2$O and THF (Fig. S25 and S26 in the ESI†). In addition, the CPL spectra of (1Ph-B-BODIPY)$_m$ were seen only in the red region (from *ca.* 500 to 700 nm). The g_{lum} value of (1Ph-B-BODIPY)$_m$ (g_{lum} = *ca.* -0.94×10^{-3} at 560 nm) was about six times smaller than that of (0Ph-B-BODIPY)$_m$ (Fig. S24B and S24C in the ESI†). These results strongly suggest the enhanced emission and CPL properties of (0Ph-B-BODIPY)$_m$ relative to (1Ph-B-BODIPY)$_m$ and (2Ph-B-BODIPY)$_m$.

Time-resolved fluorescence spectra

To examine the broadened fluorescence spectral properties of (0Ph-B-BODIPY)$_m$, time-resolved fluorescence (TRFL) spectra were measured in H$_2$O/THF (99/1, v/v).

The excitation wavelength is 404 nm. Fig. 7A shows the TRFL spectra of (0Ph-B-BODIPY)$_m$. The TRFL spectra became red-shifted with increasing time, which roughly agrees with the above-mentioned spectral shapes (Fig. 5A). Fig. 7A shows the time profiles at four different wavelengths such as 520, 610, 650, and 700 nm. The decay process becomes slower as the observed wavelength is shifted toward longer wavelengths. This means that multiple aggregate states of B-BODIPY including a monomer state are involved in the luminescence process. As stated in the Introduction section, the B-BODIPY aggregates demonstrated domino-like multi-emission processes.[40] We have performed the global analysis of the fluorescence lifetime spectra according to this result. To simplify the photophysical

Table 2 Summary of kinetic parameters in (0Ph-B-BODIPY)$_m$

k_{R1} (10^9 s^{-1})	k_{EnT1} (10^9 s^{-1})	k_{R2} (10^9 s^{-1})	k_{EnT2} (10^9 s^{-1})	k_{R3} (10^9 s^{-1})	k_{EnT3} (10^9 s^{-1})	k_{R4} (10^9 s^{-1})
0.17	10	0.20	2.6	0.22	0.42	0.25

discussion, the species-associated spectra (SAS) were measured by target analysis of TRFL spectra to analyse the excited-state species together with the proposed kinetic scheme (Scheme 1).[58,59] Based on the reported multi-emission process,[40] we assigned four different fluorescence species such as states 1–4 (Fig. 7B, C, Scheme 1, and Table 2). Note that states 1–4 in Scheme 1 represent four different aggregate states, including a monomeric state. With increasing time, multi-emission processes probably occur through energy transfer (EnT). It should be emphasized that the complicated excited-state dynamics including multi-emission exists in (0Ph-B-BODIPY)$_m$, which is one of the possible photophysical processes reflecting diversity of aggregates. Thus, we can confirm the contribution of multiple aggregate states of (0Ph-B-BODIPY)$_m$ for enhanced emission and CPL properties in the red and NIR regions.

Conclusions

In conclusion, we newly synthesized three different BINOL-substituted BODIPY derivatives and demonstrated the

2894 | *J. Mater. Chem. C*, 2023, **11**, 2889–2896

This journal is © The Royal Society of Chemistry 2023

aggregation-induced emission and circularly polarized luminescence (CPL) properties in the red and NIR regions. The steric hindrance of the phenyl groups at the 2 and 6 positions of BODIPY unit largely has an effect on the aggregate structures. In particular, (0Ph-B-BODIPY)$_m$ prepared in H_2O/THF (99/1, v/v) demonstrated the fibrous assemblies, which is in sharp contrast to the spherical assemblies of (1Ph-B-BODIPY)$_m$ and (2Ph-B-BODIPY)$_m$. The absorption and CD spectra of B-BODIPY assemblies became broadened compared to the corresponding monomeric forms. In particular, these spectra of (0Ph-B-BODIPY)$_m$ exhibited splitting signals corresponding to the 0-0 band due to the strong exciton coupling between neighboring 0Ph-B-BODIPY units together with the enhanced g_{abs} values. Moreover, (0Ph-B-BODIPY)$_m$ demonstrated a broadened fluorescence spectrum with multiple bands in the red and NIR regions, suggesting that multiple aggregate states were involved in the emission process. The CPL spectra of (0Ph-B-BODIPY)$_m$ extended up to *ca.* 800 nm and the g_{lum} value was determined to be *ca.* 5.9×10^{-3} at 638 nm. This is larger than those of 0Ph-B-BODIPY (monomer) and (1Ph-B-BODIPY)$_m$. Thus, our synthetic strategies in this study will provide a new perspective in the construction of photonics and electronics using chiral molecular assemblies.

Author contributions

T. H. designed the research; H. S. and Y. S. performed the experiments on synthesis and characterization of B-BODIPY derivatives; M. T., T. N., T. K., Y. K., and Y. H. performed the experiments and analysis on CD and CPL spectra; Y.K. and G. M. performed the experiments and analysis on XRD patterns and SAXS profiles; H. S. and T. H. wrote the manuscript. All authors reviewed and approved the manuscript.

Conflicts of interest

There are no conflicts to declare.

Acknowledgements

References

1 J. F. Sherson, H. Krauter, R. K. Olsson, B. Julsgaard, K. Hammerer, I. Cirac and E. S. Polzik, *Nature*, 2006, **443**, 557–560.

2 Y. H. Wang, H. Steinberg, P. Jarillo-Herrero and N. Gedik, *Science*, 2013, **342**, 453–457.

3 Y. J. Zhang, T. Oka, R. Suzuki, J. T. Ye and Y. Iwasa, *Science*, 2014, **344**, 725–728.

4 J. Kumar, T. Nakashima and T. Kawai, *J. Phys. Chem. Lett.*, 2015, **6**, 3445–3452.

5 Y. Sang, J. Han, T. Zhao, P. Duan and M. Liu, *Adv. Mater.*, 2020, **32**, 1900110.

6 K. Watanabe, H. Iida and K. Akagi, *Adv. Mater.*, 2012, **24**, 6451–6456.

7 E. M. Sánchez-Carnerero, F. Moreno, B. L. Maroto, A. R. Agarrabeitia, M. J. Ortiz, B. G. Vo, G. Muller and S. D. L. Moya, *J. Am. Chem. Soc.*, 2014, **136**, 3346–3349.

8 B. T. Nguyen, A. J. Ingram and G. Muller, *Chirality*, 2016, **28**, 325–331.

9 L. Zhang, T. Wang, Z. Shen and M. Liu, *Adv. Mater.*, 2016, **28**, 1044–1059.

10 J. Han, S. Guo, J. Wang, L. Wei, Y. Zhuang, S. Liu, Q. Zhao, X. Zhang and W. Huang, *Adv. Opt. Mater.*, 2017, **5**, 1700359.

11 K. Takaishi, K. Iwachido, R. Takehana, M. Uchiyama and T. Ema, *J. Am. Chem. Soc.*, 2019, **141**, 6185–6190.

12 Y. Kitagawa, M. Tsurui and Y. Hasegawa, *ACS Omega*, 2020, **5**, 3786–3791.

13 M. Hasegawa, Y. Nojima and Y. Mazaki, *ChemPhotoChem*, 2021, **5**, 1042–1058.

14 J. Gong and X. Zhang, *Coord. Chem. Rev.*, 2022, **453**, 214329.

15 X.-Y. Luo and M. Pan, *Coord. Chem. Rev.*, 2022, **468**, 214640.

16 H. Sakai, S. Shinto, J. Kumar, Y. Araki, T. Sakanoue, T. Takenobu, T. Wada, T. Kawai and T. Hasobe, *J. Phys. Chem. C*, 2015, **119**, 13937–13947.

17 H. Sakai, T. Kubota, J. Yuasa, Y. Araki, T. Sakanoue, T. Takenobu, T. Wada, T. Kawai and T. Hasobe, *Org. Biomol. Chem.*, 2016, **14**, 6738–6743.

18 H. Sakai, T. Kubota, J. Yuasa, Y. Araki, T. Sakanoue, T. Takenobu, T. Wada, T. Kawai and T. Hasobe, *J. Phys. Chem. C*, 2016, **120**, 7860–7869.

19 Y. Yamamoto, H. Sakai, J. Yuasa, Y. Araki, T. Wada, T. Sakanoue, T. Takenobu, T. Kawai and T. Hasobe, *J. Phys. Chem. C*, 2016, **120**, 7421–7427.

20 Y. Yamamoto, H. Sakai, J. Yuasa, Y. Araki, T. Wada, T. Sakanoue, T. Takenobu, T. Kawai and T. Hasobe, *Chem. – Eur. J.*, 2016, **22**, 4263–4273.

21 H. Ito, H. Sakai, Y. Okayasu, J. Yuasa, T. Mori and T. Hasobe, *Chem. – Eur. J.*, 2018, **24**, 16889–16894.

22 K. Dhbaibi, L. Favereau, M. Srebro-Hooper, M. Jean, N. Vanthuyne, F. Zinna, B. Jamoussi, L. Di Bari, J. Autschbach and J. Crassous, *Chem. Sci.*, 2018, **9**, 735–742.

23 K. Miki, T. Noda, M. Gon, K. Tanaka, Y. Chujo, Y. Mizuhata, N. Tokitoh and K. Ohe, *Chem. – Eur. J.*, 2019, **25**, 9211–9216.

24 G. Park, H. Kim, H. Yang, K. R. Park, I. Song, J. H. Oh, C. Kim and Y. You, *Chem. Sci.*, 2019, **10**, 1294–1301.

25 S. Míguez-Lago, I. F. A. Mariz, M. A. Medel, J. M. Cuerva, E. Maçôas, C. M. Cruz and A. G. Campaña, *Chem. Sci.*, 2022, **13**, 10267–10272.

This journal is © The Royal Society of Chemistry 2023

J. Mater. Chem. C, 2023, **11**, 2889–2896 | **2895**

26 Y.-F. Wu, S.-W. Ying, L.-Y. Su, J.-J. Du, L. Zhang, B.-W. Chen, H.-R. Tian, H. Xu, M.-L. Zhang, X. Yan, Q. Zhang, S.-Y. Xie and L.-S. Zheng, *J. Am. Chem. Soc.*, 2022, **144**, 10736–10742.

27 Y. Nakai, T. Mori and Y. Inoue, *J. Phys. Chem. A*, 2012, **116**, 7372–7385.

28 Y. Nakakuki, T. Hirose and K. Matsuda, *J. Am. Chem. Soc.*, 2018, **140**, 15461–15469.

29 T. Mori, *Chem. Rev.*, 2021, **121**, 2373–2412.

30 K. Mori, T. Murase and M. Fujita, *Angew. Chem., Int. Ed.*, 2015, **54**, 6847–6851.

31 N. Boens, V. Leen and W. Dehaen, *Chem. Soc. Rev.*, 2012, **41**, 1130–1172.

32 H. Lu, J. Mack, Y. Yang and Z. Shen, *Chem. Soc. Rev.*, 2014, **43**, 4778–4823.

33 T. Kowada, H. Maeda and K. Kikuchi, *Chem. Soc. Rev.*, 2015, **44**, 4953–4972.

34 J. A. Peterson, C. Wijesooriya, E. J. Gehrmann, K. M. Mahoney, P. P. Goswami, T. R. Albright, A. Syed, A. S. Dutton, E. A. Smith and A. H. Winter, *J. Am. Chem. Soc.*, 2018, **140**, 7343–7346.

35 L. Chen, D. Chen, Y. Jiang, J. Zhang, J. Yu, C. C. DuFort, S. R. Hingorani, X. Zhang, C. Wu and D. T. Chiu, *Angew. Chem., Int. Ed.*, 2019, **58**, 7008–7012.

36 W. Wan, M. S. Silva, C. D. McMillen, S. E. Creager and R. C. Smith, *J. Am. Chem. Soc.*, 2019, **141**, 8703–8707.

37 J. Gemen, J. Ahrens, L. J. W. Shimon and R. Klajn, *J. Am. Chem. Soc.*, 2020, **142**, 17721–17729.

38 Y. Hong, J. W. Y. Lam and B. Z. Tang, *Chem. Soc. Rev.*, 2011, **40**, 5361–5388.

39 C. F. A. Gomez-Duran, R. Hu, G. Feng, T. Li, F. Bu, M. Arseneault, B. Liu, E. Peña-Cabrera and B. Z. Tang, *ACS Appl. Mater. Interfaces*, 2015, **7**, 15168–15176.

40 D. Tian, F. Qi, H. Ma, X. Wang, Y. Pan, R. Chen, Z. Shen, Z. Liu, L. Huang and W. Huang, *Nat. Commun.*, 2018, **9**, 2688.

41 S. Zhang, Y. Wang, F. Meng, C. Dai, Y. Cheng and C. Zhu, *Chem. Commun.*, 2015, **51**, 9014–9017.

42 R. B. Alnoman, S. Rihn, D. C. O'Connor, F. A. Black, B. Costello, P. G. Waddell, W. Clegg, R. D. Peacock, W. Herrebout, J. G. Knight and M. J. Hall, *Chem. – Eur. J.*, 2016, **22**, 93–96.

43 J. Jiménez, C. Díaz-Norambuena, S. Serrano, S. C. Ma, F. Moreno, B. L. Maroto, J. Bañuelos, G. Muller and S. de la Moya, *Chem. Commun.*, 2021, **57**, 5750–5753.

44 M. Işık, E. Dündar, E. Şahin and C. Tanyeli, *Chem. Commun.*, 2022, **58**, 7188–7191.

45 F. Jin, J. Ye, L. Hong, H. Lam and C. Wu, *J. Phys. Chem. B*, 2007, **111**, 2255–2261.

46 A. Häbich, W. Ducker, D. E. Dunstan and X. Zhang, *J. Phys. Chem. B*, 2010, **114**, 6962–6967.

47 N. F. Bunkin, A. V. Shkirin, G. A. Lyakhov, A. V. Kobelev, N. V. Penkov, S. V. Ugraitskaya and E. E. Fesenko Jr., *J. Chem. Phys.*, 2016, **145**, 184501.

48 X. Huang, Z. Li, Y. Deng, W. Cai, L. Gu and H. Lu, *J. Phys. Chem. C*, 2020, **124**, 13966–13975.

49 A. S. D. Sandanayaka, Y. Araki, T. Wada and T. Hasobe, *J. Phys. Chem. C*, 2008, **112**, 19209–19216.

50 J. Strahan, B. C. Popere, P. Khomein, C. A. Pointer, S. M. Martin, A. N. Oldacre, S. Thayumanavan and E. R. Young, *Dalton Trans.*, 2019, **48**, 8488–8501.

51 J. Jiménez, L. Cerdán, F. Moreno, B. L. Maroto, I. García-Moreno, J. L. Lunkley, G. Muller and S. de la Moya, *J. Phys. Chem. C*, 2017, **121**, 5287–5292.

52 L. Gartzia-Rivero, E. M. Sánchez-Carnerero, J. Jiménez, J. Bañuelos, F. Moreno, B. L. Maroto, I. López-Arbeloa and S. de la Moya, *Dalton Trans.*, 2017, **46**, 11830–11839.

53 Y. Zhang, Z. Geng, Y. Zhang, Z. Xu, H. Li, Y. Cheng and Y. Quan, *J. Phys. Chem. Lett.*, 2021, **12**, 3767–3772.

54 Q. Cheng, A. Hao and P. Xing, *ACS Nano*, 2022, **16**, 6825–6834.

55 T. Nishikawa, S. Kitamura, M. Kitamatsu, M. Fujiki and Y. Imai, *ChemistrySelect*, 2016, **1**, 831–835.

56 S. Ito, K. Ikeda, S. Nakanishi, Y. Imai and M. Asami, *Chem. Commun.*, 2017, **53**, 6323–6326.

57 D. Ishikawa, T. Mori, Y. Yonamine, W. Nakanishi, D. L. Cheung, J. P. Hill and K. Ariga, *Angew. Chem., Int. Ed.*, 2015, **54**, 8988–8991.

58 I. H. M. van Stokkum, D. S. Larsen and R. van Grondelle, *Biochim. Biophys. Acta*, 2004, **1657**, 82–104.

59 J. J. Snellenburg, S. Laptenok, R. Seger, K. M. Mullen and I. H. M. van Stokkum, *J. Stat. Softw.*, 2012, **49**, 1–22.

2896 | *J. Mater. Chem. C*, 2023, **11**, 2889–2896

This journal is © The Royal Society of Chemistry 2023